Submicrometer-Resolution Mapping of Ultraweak 355-nm Absorption in HfO$_2$ Monolayers Using Photothermal Heterodyne Imaging

Introduction

Thin-film coatings for near-ultraviolet (UV), nanosecond (ns)-pulse–laser applications are usually comprised of metal oxide as the high-index component and silica oxide as the low-index material. High-resolution studies of laser-damage morphology[1] reveal two important facts about ns-pulsed–laser damage in these coatings: First, metal oxide is the weakest part and is where damage is initiated. Second, at close-to-threshold conditions, damage takes the form of submicrometer-sized craters. Such morphology indicates that the damage process starts at isolated sites and can be linked to localized absorbers, like few-nanometer–sized metal clusters,[2] or high-density electronic defect areas. Deposition of metal oxide using metal as a starting material provides the possibility for cluster formation. On the other hand, electronic defects are always present in metal-oxide dielectric materials, even in bulk form.[3] In thin-film coatings, characterized by columnar structure and large internal surfaces, submicrometer-scale electronic defect density enhancements might be expected. Clarification of the exact nature and distribution of damage precursors is essential for further improvements in damage resistance of coating materials. In this work, we make an attempt to evaluate spatial distribution of absorbers in hafnia (HfO$_2$) monolayers by using photothermal heterodyne imaging (PHI).[4] High sensitivity to absorption and true submicrometer resolution of this technique, developed specifically for nanoscale absorber detection and characterization, was demonstrated[4,5] by imaging embedded gold nanoparticles with the smallest diameter of 1.4 nm. To gain insight into the damage mechanism, our present study of PHI mapping of hafnia monolayers before and after laser irradiation is complemented by atomic force microscopy (AFM) analysis of damage morphology. This article is organized as follows: first, we describe the PHI principle, setup for sample mapping, and system calibration; then sample preparation and characterization, followed by the results of PHI mapping of differently prepared HfO$_2$ monolayers prior to laser irradiation. Next, we present the results of damage-site mapping using PHI and AFM and discuss possible damage mechanisms and the nature of damage-initiating absorbers. Finally, the conclusions are presented.

Experimental

1. The PHI Principle and Setup

Like other versions of photothermal techniques, PHI relies on the presence of a modulated pump beam that causes local modulated heating of the material and of a probe beam that experiences modification (deflection, focusing, scattering, etc.) while passing through the heated volume. In the case of PHI (see Fig. 125.23), both the pump and probe beams are focused into an overlapping, very tight, preferably diffraction limited spot inside the material. A very small absorbing defect, being covered by such a spot, heats up and, by heat conduction, causes the temperature T to rise in the surrounding host material. This process leads to a variation in the host refractive index n according to $n = n(T)$ and, consequently, probe light scattering. Moreover, because of scatterer-size modulation, the probe laser's frequency ω is shifted by an amount equal to the modulation frequency Ω. Following the description in Ref. 5, the interference between scattered and propagating (or reflected, for back configuration) probe light in the far field creates a beat signal with intensity $I(\Omega)$:

$$I(\Omega) \sim I_{\text{pump}} I_{\text{probe}}\, n \partial n \big/ \partial T \lambda^{-2} w^{-1} F(\Omega),$$

where I_{pump} and I_{probe} are the pump and probe intensities, λ and w are the probe wavelength and beam waist, respectively, and $F(\Omega)$ is a function describing heat conduction.

The experimental setup for PHI is shown in Fig. 125.24. A diode-pumped, continuous-wave (cw) semiconductor laser operating at 355-nm, 40-mW maximum output power (6 mW on sample) served as the pump laser, and a HeNe laser [633 nm, 10 mW (5 mW on sample)] was used as the probe. An acousto-optic modulator provided pump modulation in the frequency range of 100 kHz to 1 MHz, and only one beam diffracted into the first order was used as a pump. Pump and probe beams were combined at the entrance of the 40×, 0.95-N.A. (numerical aperture) microscope objective focusing both beams onto the sample mounted on the nanopositioning stage (Physik Instrumente). The stage had a minimum lateral step size of 10 nm, a maximum scan size of 200 μm, and an axial displacement of

20 μm. Probe light can be collected by either the same objective (back configuration) or an additional lens (forward configuration) and detected by a fast photodiode, lock-in amplifier (30-ms integration time), and a LabView-based data acquisition system. In the case of a back configuration, a quarter-wave plate and polarizing beam splitter were added to isolate the signal beam from the source. A detailed analysis of signals detected in either configuration can be found in Ref. 5. In this work, most measurements were performed using a forward configuration and 350-kHz modulation frequency.
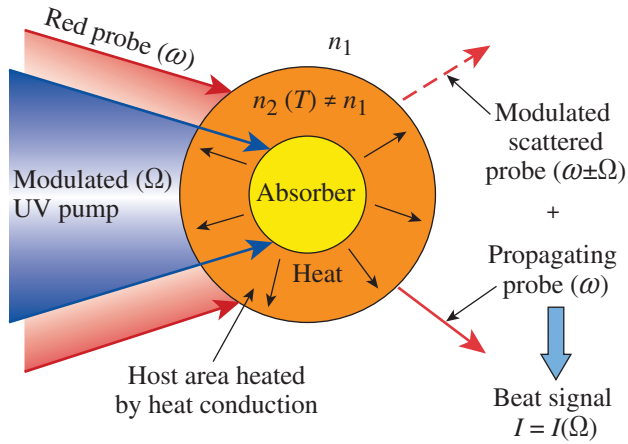
G9131JR

Figure 125.23
Schematic of photothermal heterodyne signal formation.

2. PHI-Setup Characterization and Calibration

Pump- and probe-beam focus spots were combined and characterized using a 1-μm pinhole in a metal foil. The pinhole was mounted on the nanopositioning stage using a sample holder and scanned across the beam. A corresponding image of the pump and probe beams' combined focal spot is shown in Fig. 125.25. A cross section through this image gives a full-width-at-half-maximum (FWHM) value of 0.79 μm, which should be considered an upper limit because of the transfer function of the pinhole. We estimated a real FWHM value ~10% to 15% smaller, or ~0.7 μm. Using this beam size and a maximum UV power on the sample of 6 mW, maximum power densities on the sample did not exceed ~1.6 MW/cm^2. For the system's spatial resolution and sensitivity characterization, we used 5- to 14-nm-diam isolated gold nanoparticles embedded inside silica film.[6] Figure 125.26 presents a 6-μm PHI scan and cross-sectional data for a sample with 14-nm particles, which show that a single particle is imaged as a feature with FWHM = 0.42 μm and that two particles separated by 0.55 μm can be clearly resolved. Also, particles as small as 5 nm were imaged using this setup. These calibration results proved both the true submicron spatial resolution and high sensitivity of the system. To characterize setup response in the case of homogeneous absorption, a TiO$_2$ film of ~200-nm thickness and 49% transmission at 355 nm was deposited on a fused-silica substrate. Figure 125.27 shows PHI signal dependence as a function of the pump laser's output power. It should be
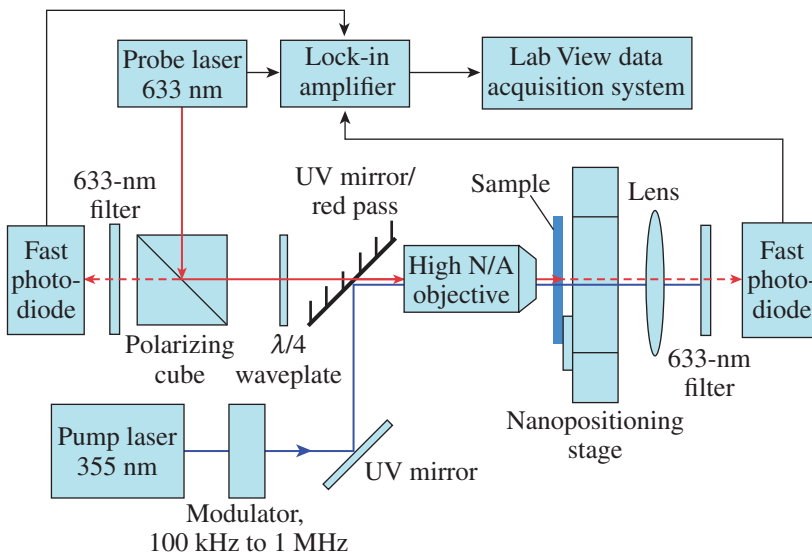
G9132JR

Figure 125.24
PHI setup for signal detection in a forward and backward configuration.

noted here that starting with powers of a few mW or higher, the signal declined as the exposure time was increased. Data shown in Fig. 125.27 were taken right after the beam shutter was opened. This effect can be attributed to some kind of sample bleaching during exposure. Consequently, it indicates that a strongly absorbing TiO_2 film is not the best solution to calibrate systems that rely on tightly focused beams. Still, with

a measured noise level of 0.5 μV and maximum PHI signal detected ~6000 μV, the signal-to-noise ratio was >10^4, which proves the high sensitivity of this PHI setup.

3. HfO₂ Sample

HfO_2 thin-film monolayer coatings, 179 nm thick (1-wave optical thickness at 355 nm), were deposited by electron-beam (e-beam) evaporation using either conventional or plasma-assisted (argon/oxygen mixture) deposition. The conventional e-beam deposition rate was 1.2 Å/s and the oxygen pressure was 8×10^{-5} Torr; in the case of the plasma-assisted deposition, the rate was –0.8 Å/s and the plasma source was operated at 180 V, 35 A. The latter was deliberately not optimized in order to produce samples with varying absorption for the same film thickness. In addition, 45-nm-thick (1/4-wave) HfO_2 film was prepared by conventional e-beam deposition to investigate PHI signal variation with film thickness. To create insulation from defects introduced by the polishing process, UV-grade
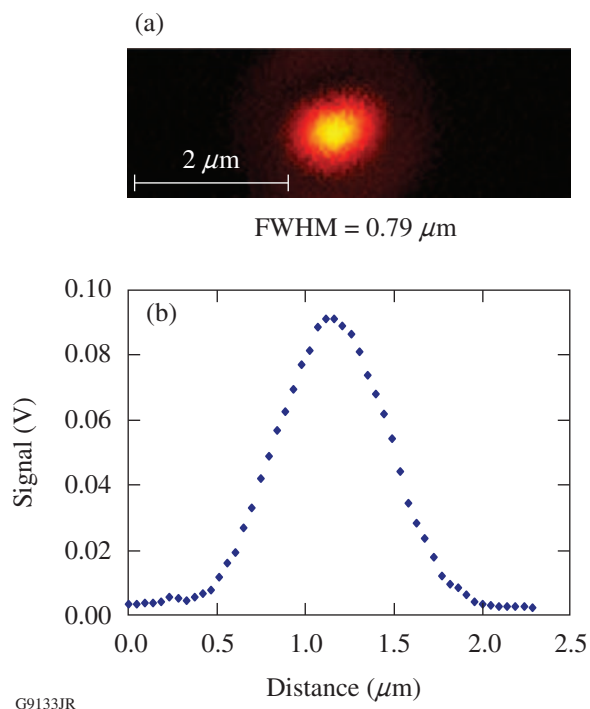
Figure 125.25
Characterization of the combined focal spot of 355-nm pump and 633-nm probe beams: (a) image of the focal spot obtained with a 1-μm pinhole; (b) cross-sectional profile.
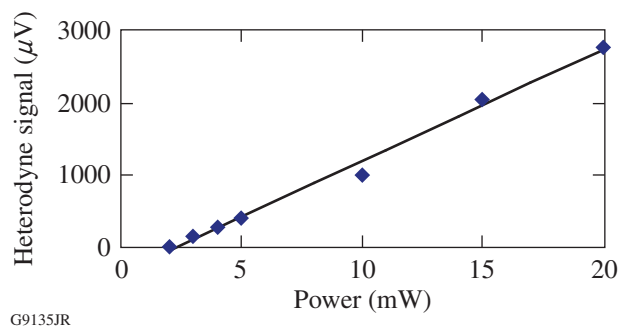
Figure 125.27
PHI signal from homogeneously absorbing TiO_2 thin-film sample as a function of 355-nm pump output power.
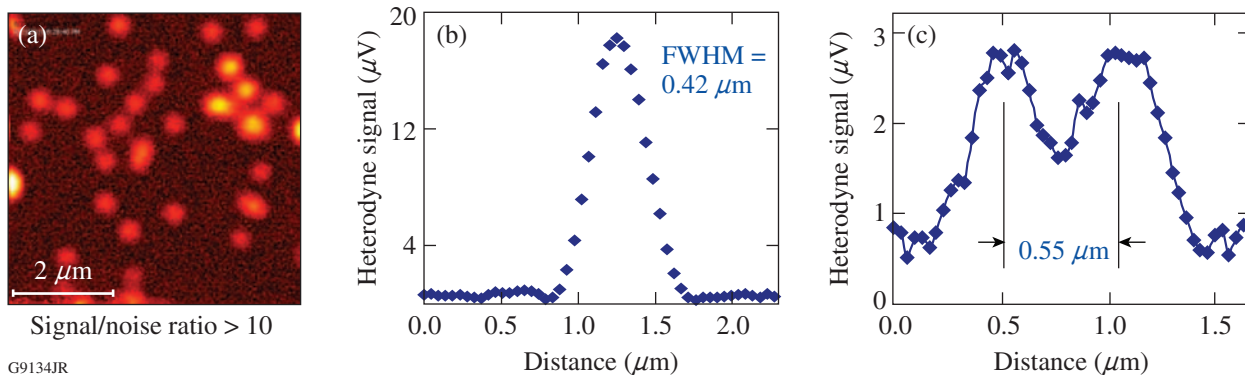
Figure 125.26
PHI calibration using embedded 14-nm gold nanoparticles: (a) 6 × 6-μm PHI image, (b) single-particle signal profile, and (c) signal profile for two particles separated by 0.55 μm.

fused-silica substrates were coated first by a 1-μm-thick SiO$_2$ layer [see Fig. 125.28(a)]. Next, in the same coating run, HfO$_2$ films of appropriate thickness were deposited. The E-field intensity distribution peaked at both interfaces and in the bulk of the 1-wave-thick film [Fig. 125.28(b)] and had only one peak at the HfO$_2$/SiO$_2$ interface in the case of 1/4-wave film [Fig. 125.28(c)]. This information is important for the analysis of the PHI signal versus film-thickness variation.

4. Damage Testing and Damage Morphology

The PHI mapping of HfO$_2$ monolayers was complemented by damage-threshold and morphology studies using 351-nm, 0.5-ns pulses from a Nd-doped glass laser. Damage thresholds

(1-on-1 mode) were measured using 110× magnification, dark-field microscopy, and damage morphology was investigated by means of AFM. Note that the 355-nm wavelength of the pump laser for the PHI technique is very close to the 351-nm wavelength of the damage-test laser, which allows one to establish correlation between measured PHI signals and damage-threshold values.

Results and Discussion

1. PHI Imaging of HfO$_2$ Films Prior to Irradiation

Photothermal images of HfO$_2$ monolayer films (see Fig. 125.29) showed different absorption levels for different film thicknesses and deposition techniques but did not show
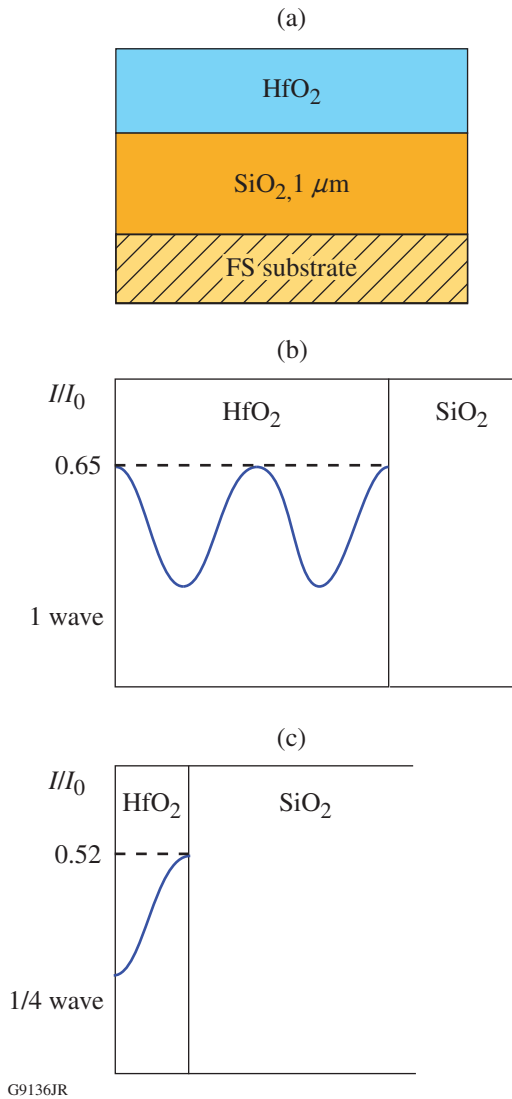
Figure 125.28
(a) Schematic of HfO$_2$ thin-film sample and E-field intensity distribution for (b) 1-wave-thick and (c) 1/4-wave-thick samples.
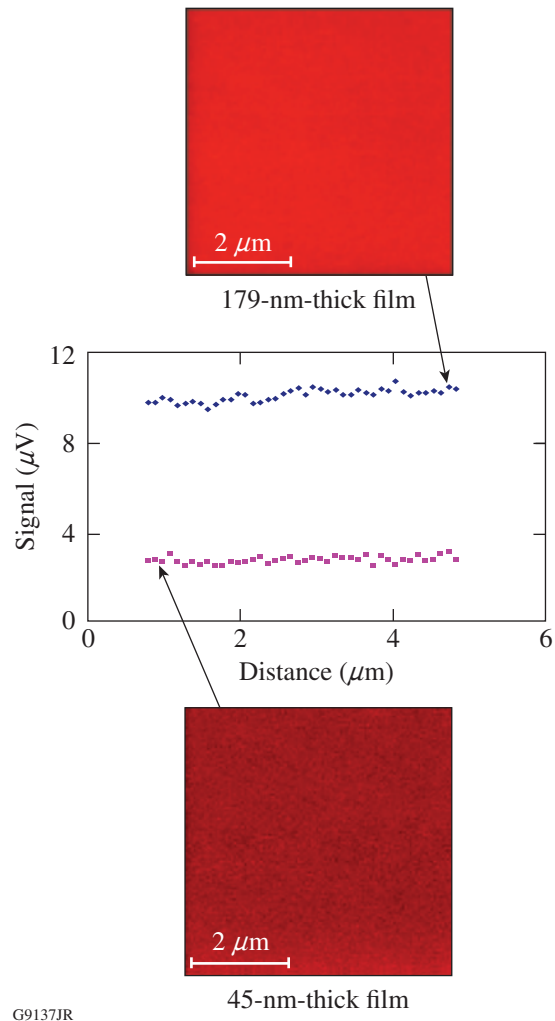
Figure 125.29
Heterodyne images and corresponding horizontal signal profiles of conventionally deposited 179-nm-thick and 45-nm-thick HfO$_2$ films prior to irradiation.

any structure attributable to the presence of isolated localized absorbers. This allows us to hypothesize that average distances between absorbing defects are much smaller than the laser beam's spot size and, moreover, than the ~0.4-μm spatial resolution of the system. Comparison of PHI signals for two different HfO$_2$ film thicknesses, 1 wave and 1/4 wave, gave a ratio very close to 4:1 (Fig. 125.29), which renders a PHI signal proportional to the film thickness and also to the absorbing volume. This important result indicates that despite the presence of the intensity peak [Figs. 125.28(b) and 125.28(c)], absorption at the HfO$_2$/SiO$_2$ interface is not a dominating factor. Otherwise, the ratio of signals should be close to 1.25, in agreement with the intensity ratio at the interface position.

As expected, a 1-wave-thick sample deposited by a plasma-assisted technique, non-optimized for a laser-damage performance, generated an almost 3× higher PHI signal compared to a standard e-beam–deposited sample. This result correlates well with single-shot damage thresholds measured for these samples (see Table 125.I) and, if confirmed by the larger statistics for different coating materials, can point to the PHI technique as a preliminary indicator of ns-pulse laser damage performance.

Table 125.I: Damage thresholds (351 nm) and corresponding PHI signals for 1-wave-thick HfO$_2$ films.

HfO$_2$ films	Damage thresholds (J/cm^2)	Heterodyne signal (μV)
Standard e-beam	3.57±0.23	9.8
Plasma assisted	2.03±0.13	27.6

2. PHI and AFM Mapping of HfO$_2$ Damage Morphology

PHI and AFM mapping of damaged sites revealed damage in the form of micrometer- and nanometer-scale craters. These craters appear as very dark (no signal) features on PHI images (Fig. 125.30). Taking into account that no signal was detected on silica samples without a hafnia layer, one can assume that the HfO$_2$ layer has been removed in the crater-formation process. Another observation is that scans performed in the central part of the damage site, and depicted in Fig. 125.30(c), show enhanced absorption in parts of the coating that survived laser irradiation. This indicates structural modification of HfO$_2$ film subjected to a fast heating and cooling cycle and allows one to forecast damage propagation under continuing pulse irradiation. PHI images of damage morphology also provided an opportunity to independently evaluate the method's spatial resolution, because of re-deposited nanoscale particles. A cross-sectional profile through one of these particulates, shown in Fig. 125.30(d), confirmed a true submicrometer resolution of 0.4 μm, in good agreement with the calibration value of 0.42 μm obtained using gold nanoparticles. AFM imaging (Fig. 125.31) revealed further details about the damage process. Both isolated craters [Fig. 125.31(a)] imaged on the periphery of the damage site and merging craters from the heavier-damaged central part of the same site [Fig. 125.31(b)] are missing the granular structure of the surrounding coating material. Such morphology indicates that a melting point has been reached by the material at the bottom of the crater (SiO$_2$, as revealed by AFM analysis), and the observed smooth, glassy structure is a result of material flow and resolidification. Moreover, crater boundaries and narrow "bridges" between
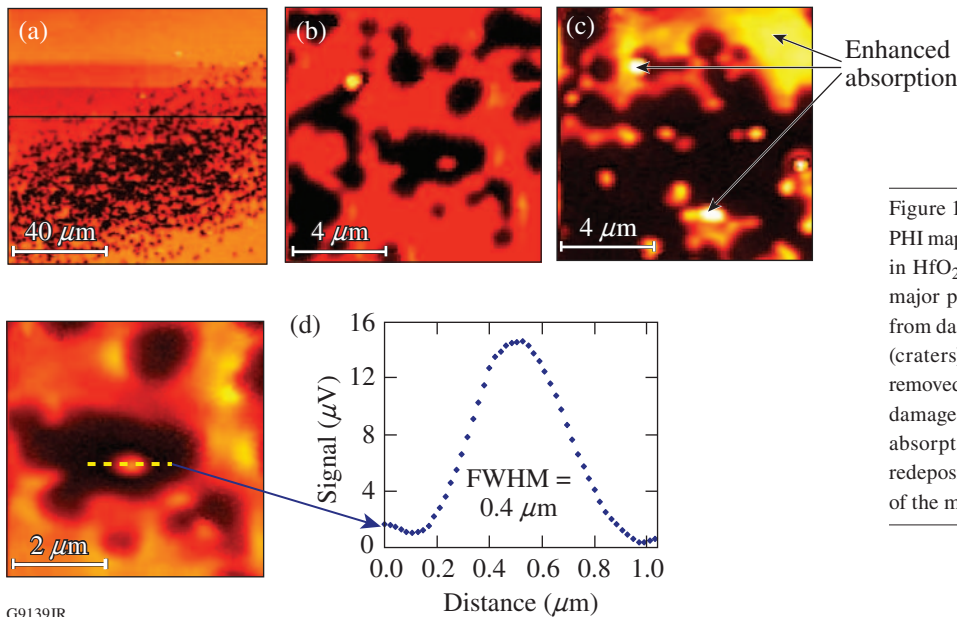
Figure 125.30
PHI mapping of 351-nm, 0.5-ns damage morphology in HfO$_2$ film samples: (a) 100-μm scan covering a major portion of the damage site; (b) 10-μm scan from damage site periphery [dark features are areas (craters) where hafnia film has been completely removed]; (c) 10-μm scan from the central part of the damage site; remaining hafnia film shows enhanced absorption; (d) cross-sectional profile through a redeposited particle, confirming 0.4-μm resolution of the method.

G9139JR

(a) (b)

10-μm scan 4-μm scan

G9138JR
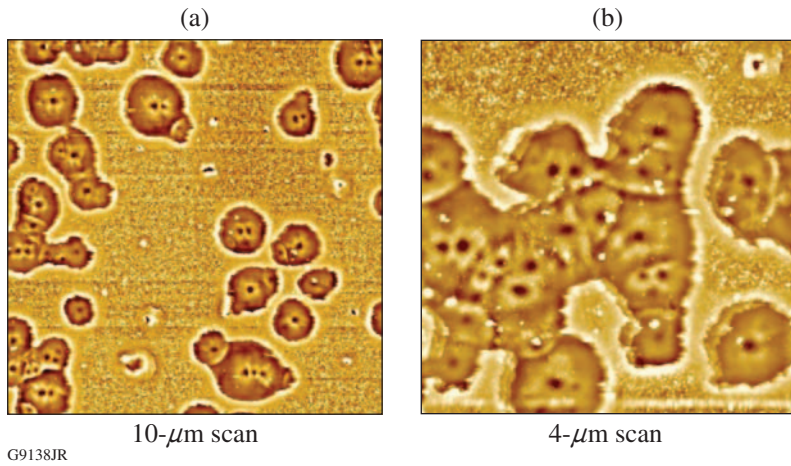
Figure 125.31
AFM images of damage morphology: (a) isolated craters formed on the damage-site periphery (10-μm scan); each crater has at least one damage origination point; (b) merging craters from the central part of the damage (4-μm scan); crater edges show smoothing of granular film structure, indicative of reaching the melting point.

craters [Fig. 125.31(b)] show HfO₂ film granularity that is much smoother than normal coating granularity, indicating the early stage of HfO₂ material melting. Small (100 nm or smaller) particles inside the area of heavier damage [presented in Fig. 125.31(b)] are attributed to material being redeposited onto the surface during crater formation. Another important observation here is that each crater [Fig. 125.31(a)] has in its central part at least one additional nanoscale protrusion—the point at which damage originates. Calculation of the average initiation-point separation using data from Fig. 125.31(b) gave a value of 272±59 nm. Previous studies using artificial nanoscale absorbers[7] demonstrated that damage initiation requires an effective energy transfer from absorber to the surrounding matrix; in porous thin-film material, only part of all absorbers can satisfy this condition. From this, we conclude that the actual distance between absorbing defects is smaller than the measured initiation-point separation. This conclusion is strongly supported by our previously derived estimate (see **PHI Imaging of HfO₂ Films Prior to Irradiation**, p. 28) that the separation would be much smaller than 0.4 μm. Consequently, we estimate the upper limit for the average absorber separation to be ~100 nm.

Cross-sectional profiles taken on AFM images (Fig. 125.32) through damage craters reveal further details of crater formation. An average crater depth of 186 nm appears to be very close to the 179-nm thickness of the HfO₂ layer, which strongly supports hafnia layer removal suggested by PHI mapping. A nanoscale protrusion located at the center of the main crater propagates 30 nm to 80 nm into the supporting SiO₂ layer, which also clearly points to localized absorption and material removal in the silica layer. Such observations suggest the following damage-process scenario: Energy from the laser pulse is initially absorbed at random locations within the HfO₂ layer, causing a local temperature rise. At selected locations, charac-

3-μm scan

G9140JR
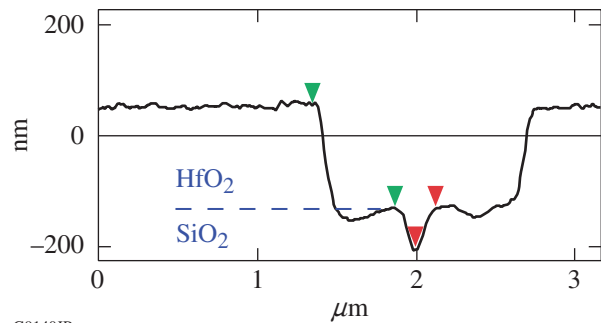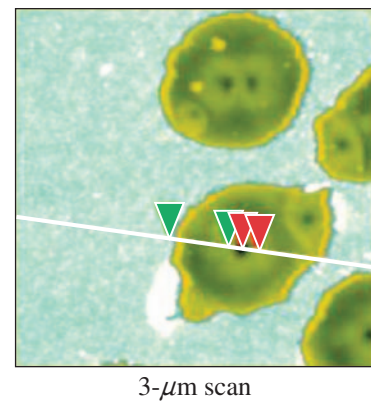
Figure 125.32
Damage crater cross-sectional profile (AFM). Crater-depth measurement points to removal of the hafnia layer within crater volume.

terized by good thermal contact between the HfO₂ and SiO₂ layers, heat conduction through the HfO₂/SiO₂ interface may raise the temperature in the SiO₂ material up to the melting point and higher. Recently, it was convincingly demonstrated[8] that silica, upon reaching a temperature $T \approx 2200$ K (slightly above melting point), becomes absorbent enough at 355 nm to cause a dramatic drop in the nanosecond-pulse surface damage threshold. In our case, it means that once this temperature

is reached inside the SiO_2 layer within the laser-pulse–length interval, local temperature and pressure can grow dramatically by acquiring energy from the laser pulse. As a result, explosive removal of the HfO_2 material within the main crater volume and SiO_2 material within the central nanocrater takes place. Taking into account that the hafnia melting point $T_m(HfO_2) = 3085$ K is much higher than that of silica, $T_m(SiO_2) = 1986$ K, HfO_2 material can be removed from the crater volume via a stress-driven mechanism, without full melting.[9] This conclusion is supported by crater morphology (see Fig. 125.32) characterized by sharp edges that are missing an elevated smooth rim, typical for melted material flow.

3. Nature of Nanoscale Absorbers

As suggested in the **Introduction**, p. 25, there are two possible nanoscale absorber candidates in metal-oxide thin film: metal clusters and high-density areas of electronic defects. Figure 125.33 shows the spectral dependence of the absorption cross section for a 10-nm Hf cluster.[10] Also on Fig. 125.33 are data for a 10-nm gold cluster calculated[10] at 355-nm wavelength, which is just slightly larger than for Hf. In **Experimental**, p. 25, we reported on PHI imaging of gold clusters as small as 5 nm, making it realistic to assume that we could detect similarly sized Hf clusters using PHI, if the same were present in the HfO_2 film. Assuming ~100-nm average separation between 5-nm clusters, lattice unit cell volumes[3] of 2.23×10^{-2} nm³ for Hf, and 3.48×10^{-2} nm³ for HfO_2, the portion of Hf in a form of clusters inside HfO_2—3.1×10^{-5}—is rather high. Another
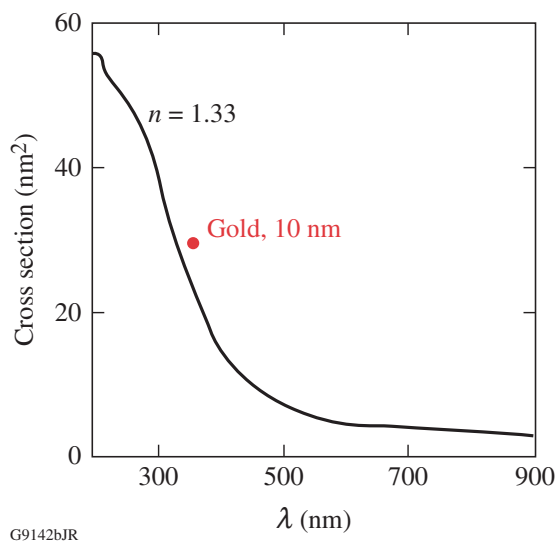
observation that questions the possible role of metal clusters is that HfO_2 films deposited from oxide, as a starting material, should have a lower probability of metal-cluster formation than films deposited from Hf metal. Nevertheless, films produced by oxide evaporation show higher absorption and lower UV–ns-pulse damage thresholds.[11] Thermodynamic modeling of cluster formation in an evaporation plume and also during film growth is needed to evaluate the realistic cluster fraction inside metal oxide film.

Absorption by electronic defects, enhanced at grain boundaries within columnar film structure, is another possible source of damage initiation. Photoluminescence excited by 266-nm, 4.66-eV photons revealed a rich spectrum attributable to absorption from electronic defect states.[11] Figure 125.34 shows an energy diagram for oxygen-ion vacancy defect states (V^+ and V^{2+}) inside a HfO_2 bandgap,[3] where energy permits electron transition into the conduction band by absorption of 355-nm, 3.5-eV photons. Further heating of these electrons by a laser pulse ensures avalanche formation and damage. For obvious reasons, spatial density of the electronic defects must be much larger than cluster density in order to achieve a similar localized effect. That might explain the very small spatial signal variation on PHI images of HfO_2 films prior to irradiation as a result of averaging over a large number of absorbing defects. Further experiments and modeling are needed to clarify which type of absorbing defect plays a major role in the damage process.

G9142bJR

Figure 125.33
Absorption cross section for 10-nm-diam Hf cluster in a medium with refractive index = 1.33 as a function of wavelength. For comparison, 355-nm–wavelength data for a 10-nm Au cluster are also shown on the graph.

G9142aJR
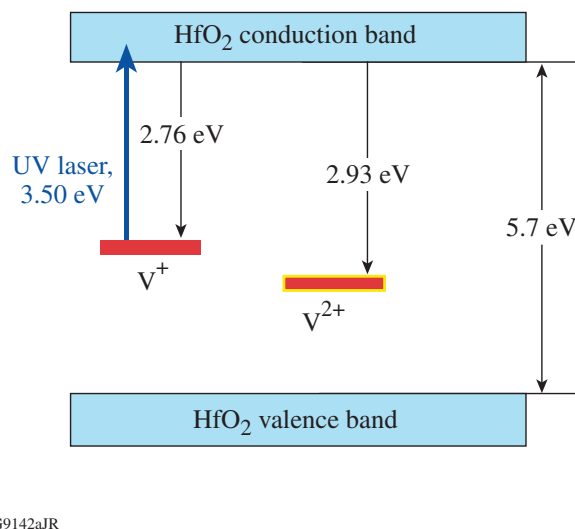
Figure 125.34
Energy-level diagram for defect states[3] in monoclinic HfO_2 whose electron affinities permit electron excitation into the conduction band through absorption of a 355-nm photon.

Conclusions

Photothermal heterodyne imaging using near-UV light as a pump source can measure metal oxide's thin-film absorption properties with high sensitivity and submicron ($\sim$0.4-μm) spatial resolution.

PHI images of HfO$_2$ films prior to irradiation are structureless, pointing to absorber separations much smaller than the 0.4-μm resolution of this method. Combining these data with damage initiation statistics allowed us to estimate an upper limit for an average absorber separation at $\sim$100 nm. By comparing heterodyne signals for different film thicknesses, we found that HfO$_2$/SiO$_2$ interfacial absorption is not a major factor, but the main contribution comes from absorption inside HfO$_2$ film.

Observed correlation between PHI signals and measured nanosecond-pulse damage thresholds for HfO$_2$ monolayer films points to PHI as a useful technique for predicting laser-damage resistance of differently deposited thin films.

Using AFM and PHI to analyze the damage morphology allowed us to suggest a HfO$_2$ damage mechanism. The process starts with localized absorption and a temperature rise in the HfO$_2$ film and is followed by heat transfer to the supporting SiO$_2$ layer by means of heat conduction. At locations with good thermal contact, the temperature in SiO$_2$ can rise above the melting point and reach a critical temperature $\sim$2200 K at which silica transforms into an effectively absorbing material. As a result, energy acquisition from the laser pulse leads to a quick temperature and pressure rise, explosive material removal, and damage.

Hafnium clusters and high-density areas of electronic defects still remain hypothetical candidates as damage initiators. Further experiments and modeling are required for unambiguous damage-driving absorber identification.

REFERENCES

1. S. Papernov and A. W. Schmid, J. Appl. Phys. **82**, 5422 (1997).

2. S. Papernov, A. W. Schmid, A. L. Rigatti, J. B. Oliver, and J. D. Howe, in *Laser-Induced Damage in Optical Materials: 2005*, edited by G. J. Exarhos *et al.* (SPIE, Bellingham, WA, 2005), Vol. 5991, pp. 429–435.

3. A. S. Foster *et al.*, Phys. Rev. B **65**, 174117 (2002).

4. S. Berciaud *et al.*, Phys. Rev. Lett. **93**, 257402 (2004).

5. S. Berciaud *et al.*, Phys. Rev. B **73**, 045424 (2006).

6. S. Papernov and A. W. Schmid, J. Appl. Phys. **104**, 063101 (2008).

7. S. Papernov and A. W. Schmid, J. Appl. Phys. **92**, 5720 (2002).

8. J. Bude *et al.*, in *Laser-Induced Damage in Optical Materials: 2007*, edited by G. J. Exarhos *et al.* (SPIE, Bellingham, WA, 2007), Vol. 6720, p. 672009.

9. S. I. Kudryashov, S. D. Allen, S. Papernov, and A. W. Schmid, Appl. Phys. B **82**, 523 (2006).

10. J. A. Creighton and D. G. Eadon, J. Chem. Soc. Faraday Trans. **87**, 3881 (1991).

11. A. Ciapponi *et al.*, J. Lumin. **1029**, 1786 (2009).